Journal of Materials Chemistry C

ROYAL SOCIETY OF CHEMISTRY

PAPER

View Article Online
View Journal | View Issue

Open Access Article. Published on 22 September 2025. Downloaded on 1/19/2026 9:23:49 PM.
This article is licensed under a Creative Commons Attribution 3.0 Unported Licence.

Check for updates

Cite this: J. Mater. Chem. C, 2025, 13, 22207

Interfacial electronic structure modulation by facet orientation and sulfur vacancies in CdS/MoS_2 heterojunctions

Beniam Kumela, Roozbeh Anvari and Wennie Wang *

Received 23rd June 2025,
Accepted 9th September 2025

DOI: 10.1039/d5tc02423d

rsc.li/materials-c

We investigate how facet orientation and sulfur vacancies influence the interfacial charge transfer properties of CdS/MoS_2 heterojunctions. Using density functional theory, we find that the (001)-CdS/MoS_2 interface exhibits a type-III band alignment, while the (100)-CdS/MoS_2 forms a homojunction-like alignment that straddles the water redox potentials, making it more suitable for overall water splitting. Furthermore, sulfur vacancies induce localized charge redistribution at the (100)-CdS/MoS_2 interface, with select configurations introducing shallow defect states that may aid in the charge transfer pathways of hydrogen evolution reactions through favorably aligned dipole moments. In contrast, sulfur vacancy configurations in the (001)-CdS/MoS_2 interface produce a more uniform charge redistribution and minimal changes in the electronic structure. The resulting dipole moments in the (001)-CdS/MoS_2 may instead limit the desired interfacial charge transfer. Finally, we find that defect formation energy differences reveal a facet-dependent tendency to form sulfur vacancies in CdS/MoS_2.

1 Introduction

Continuously growing hydrogen demand has been predominantly met through non-renewable sources, underscoring the urgent need for sustainable production alternatives.[1–3] Photocatalytic water splitting utilizes sunlight to drive hydrogen production, offering a green alternative that may circumvent the high costs associated with electrolysis systems, such as the reliance on rare earth catalysts[4] and extensive electrical infrastructure requirements.[5,6]

To improve the efficiency of photocatalysis, research is focused on materials that minimize charge carrier recombination[7] and utilize the high irradiance, visible range of light (1.63–3.26 eV).[8] Among several candidates, cadmium sulfide (CdS) shows great promise as its bulk crystal has a band gap of 2.42 eV[9] and is comprised of earth abundant constituents. However, CdS photocatalytic performance is known to suffer from significant photocorrosion[10,11] and recombination.[12]

Several experiments have observed heterojunction photocatalysts as a path to resolve the shortcomings of CdS.[13] At a heterojunction interface, dissimilar energy alignment of the band edges results in charge carrier transport across the two materials. If the bands form a staggered (type-II) alignment, this can result in charge carrier separation which reduces recombination and enhances photocatalytic efficiency. Zong *et al.* found that loading MoS_2 onto CdS yields the highest photocatalytic activity compared to loading with noble metals.[14] This is particularly interesting because platinum (Pt), one of the co-catalysts tested, is well known to outperform MoS_2 as a promoter for H_2 evolution in electrochemical systems, a trend explained by its position near the peak of the volcano plot relating exchange current density to the free energy of adsorption of hydrogen.[15] Thus, the authors suggest that the heterojunction formed between MoS_2 and CdS is important for enhancing the photocatalytic activity. Although a

McKetta Department of Chemical Engineering, The University of Texas at Austin, USA. E-mail: wwwennie@che.utexas.edu

Wennie Wang

Wennie Wang is a computational materials scientist and current assistant professor in the McKetta Department of Chemical Engineering at the University of Texas at Austin. She earned her BS degree in Materials Science and Engineering from the Massachusetts Institute of Technology in 2013, followed by her PhD in Materials at the University of California, Santa Barbara, in 2018 and a postdoctoral appointment at the University of Chicago in the Pritzker School of Molecular Engineering. Her research leverages first-principles computational methods for studying the optical and electronic properties of semiconductors, with a particular emphasis on defects in transition metal compounds.

Open Access Article. Published on 22 September 2025. Downloaded on 1/19/2026 9:23:49 PM.
This article is licensed under a Creative Commons Attribution 3.0 Unported Licence.

performance increase has been observed with MoS_2, the mechanism behind this enhancement remains unclear. Liu *et al.* reported an increase in incident photon-to-current efficiency (IPCE) and a reduction in photoluminescence (PL) for CdS loaded with MoS2.[16] Based on Mott–Schottky (M–S) analysis, they proposed that the improved efficiency arises from reduced recombination, which is attributed to charge separation resulting from the formation of p–n heterojunctions. Min *et al.* observed that the increase in CdS/MoS_2 photocatalytic activity is sustained after more than 4 hours of irradiation.[17] This led them to propose the formation of a type-I band alignment facilitating hole transfer from CdS to MoS_2 and causing the MoS_2 to act as a sacrificial agent that inhibits CdS corrosion. Conversely, Ma *et al.* observed CdS corrosion in CdS/MoS_2 during stable H_2 production.[18] Using heterogeneous nucleation theory, they proposed that sulfur vacancies on MoS_2 serve as recrystallization sites for degraded CdS ions, corroborated by similar observations in CdS/WS_2.[19]

In parallel to experiments, several first-principles studies attempt to further elucidate the mechanisms behind the efficiency of CdS/MoS_2. Modeling the cubic-CdS/MoS_2 system using mono-layers within the density functional theory (DFT) framework, Lian *et al.* found that the interface resembles a p–n heterojunction with a built-in potential of 0.45 eV, which could be responsible for the observed electron–hole separation.[20] Zhang *et al.* compared the (001) and (100)-CdS/MoS_2 heterostructures with a monolayer or bilayer of CdS to find that (100)-CdS/MoS_2 exhibits more favorable properties for photocatalytic performance, such as a stronger binding energy, expanded light absorption edge, and faster hole migration speed.[21] Using time-dependent density functional theory (TDDFT), Cheng *et al.* identified two sequential mechanisms—electron–phonon coupling and interfacial dipole-driven state alignment—that govern charge separation in (001)-CdS/MoS_2, leading to gradual then rapid electron transfer across the interface.[22]

Although previous studies have highlighted several important mechanisms by which CdS/MoS_2 heterojunctions enhance their photocatalytic efficiency, several critical effects remain unaddressed or only partially considered. As previously noted, the exact nature of the heterojunction observed in experiments remains uncertain, with various studies reporting a homojunction,[16] type-I,[23–25] or type-II[26,27] band alignments. A possible explanation for these discrepancies lies in the fact that several studies have determined band alignment based on band edges of isolated CdS and monolayer MoS_2, prior to heterojunction formation. However, these band edges can shift upon heterojunction formation due to interfacial dipole moments and strain – though the direction and magnitude of this shift remain unexplored for the CdS MoS_2 interface. To the best of our knowledge, no prior computational studies have modeled full slab representations of both experimentally relevant CdS facets – (001) and (100)[28] – in contact with MoS_2.

The role of the interfacial defects in CdS/MoS_2 is also under explored. Vacancies and other intrinsic defects can enhance light absorption by introducing mid-gap states, which enable sub-bandgap photon excitation and broaden the absorption spectrum.[29] These defect states have been proposed to improve charge separation by acting as temporary trapping sites for photo-generated carriers, thereby reducing the probability of direct electron–hole recombination.[30] Sulfur vacancies in MoS_2 have been shown to activate the otherwise inert basal plane for the hydrogen evolution reaction (HER) by tuning the free energy of adsorption of hydrogen closer to 0 at specific concentrations.[31,32] This not only enhances catalytic activity but also improves charge utilization by facilitating electron transfer to adsorbed hydrogen intermediates. However, the role of defects at the interface has seen limited study. To address these gaps, we systematically investigate changes in band alignment at the CdS/MoS_2 heterojunction, the effects of interfacial dipole formation, and the impact of point defects on the electronic structure and charge redistribution. To do this, we use full slab models of experimentally relevant CdS facets interfaced with monolayer MoS_2 with and without sulfur vacancies. This approach will lead to a deeper understanding of the mechanisms that enhance photocatalytic efficiency in CdS/MoS_2. This paper is organized as follows. In Section 2, we detail our computational methodology used to model CdS/MoS_2. In Section 3.1, we discuss electronic properties of the individual CdS surfaces and MoS2 monolayer. In Section 3.2, we examine the interfacial charge transfer and band realignment that occurs in the heterojunction. In Section 3.3, we investigate the influence of sulfur vacancies on the CdS/MoS_2 interface. Finally, Section 4 summarizes our findings and discusses their implications for understanding the mechanisms behind the enhanced photocatalytic performance of CdS/MoS_2.

2 Computational methods

In this section, we highlight the computational methodology used to model the CdS/MoS_2 heterojunction. Our structural model of the heterojunction is composed of the wurtzite phase of CdS and monolayer 2H phase of MoS_2. To construct the interface, we first optimize the bulk lattice constants of both materials. The resulting values are consistent with previous first-principles and experimental studies as shown in Table S1.[33–36]

Using these optimized lattice constants, we cleave the (100)- and (001)-CdS surfaces from the bulk crystal. Notably, the (001)-CdS surface contains 0.5 e^- per unpassivated Cd bond, making it unstable.[37] To satisfy the electron counting model,[38] we introduce one Cd vacancy per 2×2 unit cell [$c(2 \times 2)$ reconstruction]. This reconstruction is experimentally observed in similar surfaces, such as (001)-ZnSe.[39] First-principles studies further indicate that this reconstruction induces planarization around the surface Cd atoms, consistent with passivation through electron transfer.[37] In contrast, the stoichiometric (100)-CdS surface is nonpolar, requiring no such modification.

Extended surface slabs are essential for capturing bulk interactions that are absent in monolayer models and are crucial for accurately predicting the geometry, energetics, and electronic features of the surface layer.[40] To construct an accurate yet computationally efficient slab model, we vary the number of CdS atomic layers and monitor the convergence of the work function and surface energy. We find that with three atomic layers, the changes in work functions of the (100)- and (001)-CdS surfaces are

 This journal is © The Royal Society of Chemistry 2025

Open Access Article. Published on 22 September 2025. Downloaded on 1/19/2026 9:23:49 PM.
This article is licensed under a Creative Commons Attribution 3.0 Unported Licence.

below 10 meV and variations in the surface energies are less than 1 meV Å^{-2}. These values are consistent with previous first-principles and experimental studies, as summarized in Table S2.[41–44]

After determining the slab model, we interface the two materials aiming to find a small lattice mismatch (Δm) while maintaining a reasonably sized supercell. To achieve this, we systematically explored different integer multiples of the primitive surface unit cells of each material to identify pairs of supercells that closely match in-plane lattice vectors. In this study, we use a 3 × 3 (100)-CdS supercell with a 4 × 4 MoS_2 supercell resulting in Δm_x = 2.03% and Δm_y = 8.74%. For (001)-CdS, we use a 4 × 4 supercell with a 5 × 5 MoS2 supercell, which gives $\Delta m_x = \Delta m_y$ = 4.55%. We note that CdS/MoS_2 heterostructures mainly grow in nanowire and nanoparticle morphologies, which maintain coherent interfaces when lattice mismatch values are less than 10%, consistent with the values in this study.[45] Table S5 summarizes the strain experienced by MoS_2 and the associated changes in its band gap.

Sulfur vacancies are among the most common native defects in CdS/MoS_2 heterostructures, due to their low formation energies and thermodynamic stability under typical experimental growth conditions, as reported for bulk MoS_2.[35] To investigate their effects, we introduce sulfur vacancies on top of the MoS_2 monolayer facing the vacuum positioned above a Cd atom, above a S atom, and within a hollow site as highlighted in Fig. S3. To accommodate these distinct configurations in the (100)-CdS/MoS_2 system, the surface was extended in the *x*-direction, resulting in an 8 × 4 supercell for CdS and a 10 × 5 supercell for MoS_2.

First-principles electronic structure calculations based on density functional theory (DFT) were conducted using the QUANTUM ESPRESSO software package (version 7.3).[46] Calculations were performed using optimized norm-conserving Vanderbilt pseudopotentials,[47] the generalized gradient approximation for exchange correlation interactions, and Perdew–Burke–Ernzerhof (PBE) functional.[48] The DFT-D3 method is used to account for van der Waals dispersion interactions.[49] The heterostructures were placed in a vacuum of 25 Å along the *z*-axis and the atomic coordinates were relaxed with an energy cutoff of 70 Ry until the interatomic forces and energy were below 10^{-2} eV Å^{-1} and 10^{-4} Hartree, respectively. The Brillouin zone was sampled by 2 × 2 × 1 and 4 × 4 × 1 Monkhorst–Pack grids for geometry optimization and density of states, respectively. The calculation of formation energy of defects, heterostructure binding energy, dipole moment, work function, surface energy, and charge density difference are detailed in Section S0.1.

3 Results and discussions

3.1 Isolated components of the CdS/MoS_2 heterostructure

In this section, we examine the electronic properties of the CdS surfaces and MoS_2 monolayer in isolation. Upon relaxation, we find that both the (100)- and (001)-CdS surfaces undergo extensive reconstruction as depicted in Fig. S1 and quantified in Tables S3 and S4. The initially planar (100)-CdS surface becomes corrugated due to the presence of dangling bonds in the top layer. In contrast, the (001)-CdS surface exhibits planarization around the surface Cd atoms, in which the corrugated (001)-CdS surface becomes flattened upon relaxation, consistent with the previously noted effect of passivation *via* electron transfer. Although not quantified, we observe that the pristine monolayer MoS_2 remains largely unreconstructed after relaxation, in agreement with prior first-principles calculations.[50] As shown in Table S2, the (001)-CdS surface has a higher surface energy than the (100)-CdS surface (0.90 J m^{-2} *vs.* 0.28 J m^{-2}), which is consistent with previous first-principles studies on CdS surfaces.[42] Experimental observations further corroborate this, showing that CdS preferentially grows along the (001) direction—often forming nanorod-like morphologies, particularly at elevated temperatures.[27,51] This anisotropic growth is attributed to the higher reactivity of the (001) surface, which, due to its greater surface energy and higher density of dangling bonds, promotes nucleation and heteroepitaxial growth.[52]

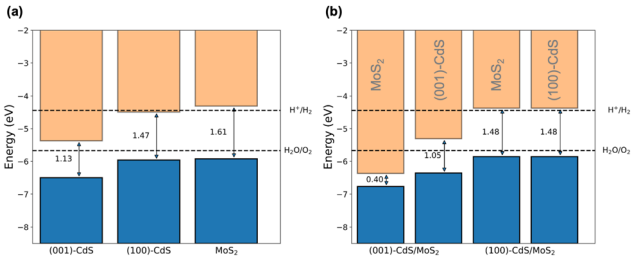

Fig. 1 Conduction (orange) and valence (blue) band edges for the (a) isolated components and (b) heterostructures with component contributions from the MoS_2 (left) and CdS surface (right) are plotted with respect to vacuum. Corresponding band gap values (in eV) are given between the band edges. The redox potentials of water are indicated by the dotted lines.

Next, we examine band edges of both CdS surfaces and mono-layer MoS_2. According to the first three columns of the diagram in Fig. 1, we anticipate that both (001)- and (100)-CdS surfaces will form a type-II heterojunction with MoS_2. The band alignment indicates that electrons transfer from MoS_2 to CdS and holes migrate from CdS to MoS_2. This spatial separation of charge carriers can suppress recombination and enhance photocatalytic efficiency. However, contrary to this expected behavior, electron accumulation on MoS_2 is actually preferred for hydrogen evolution. MoS_2 is known to be an excellent hydrogen evolution reaction (HER) catalyst due to its near-zero free energy of adsorption of hydrogen.[53–55]

3.2 Interfacial dipole formation and band alignment renormalization

In this section, we examine the interfacial charge transfer and band alignment renormalization that occur in the (001)- and (100)-CdS/MoS_2 heterojunctions. Upon relaxation, we obtain binding energies of −17.59 and −17.18 meV Å^{-2} for (001)-and (100)-CdS/MoS_2, respectively. The negative values indicate that the formation of these heterostructures is both energetically favorable and spontaneous. Moreover, the magnitude of the binding energies fall within the typical range for van der Waals

Open Access Article. Published on 22 September 2025. Downloaded on 1/19/2026 9:23:49 PM.
This article is licensed under a Creative Commons Attribution 3.0 Unported Licence.

interactions (13–21 meV Å^{-2}), suggesting that these forces dominate the interfacial adhesion.[56] This interpretation is further supported by the relatively large interlayer distances of 3.12 and 3.04 Å for (001)- and (100)-CdS/MoS_2 (as shown in Fig. S2), which are significantly greater than the equilibrium Cd–S bond length of 2.55 Å, indicating the absence of covalent bonding across the interface. We also observe that (001)-CdS/MoS_2 has a more negative binding energy, which supports selective growth behavior noted earlier.[52]

Charge redistribution at the interface leads to the formation of interfacial dipole moments, as illustrated in Fig. 2. These dipole moments induce electron accumulation on MoS_2 and CdS for the (001)- and (100)-CdS/MoS_2 heterostructures, respectively. Notably, the interfacial dipole moment in (001)-CdS/MoS_2 (-2.51×10^{-6} Debye) is three orders of magnitude greater than that of (100)-CdS/MoS_2 (1.15×10^{-9} Debye). This difference may be explained by the polar nature of the (001)-CdS surface termination, which facilitates the transfer of electrons from CdS to the electron-deficient MoS_2 layer. This charge transfer arises from an interfacial dipole that points in the opposite direction, from MoS_2 toward CdS, compared to a nonpolar interface. In contrast, the (100)-CdS surface is nonpolar, which leads to a smaller dipole moment and weaker driving force for charge transfer. This can be further understood by comparing Fig. 1 and 2. In the (001)-CdS/MoS_2 case, the MoS_2 layer screens the large intrinsic dipole of (001)-CdS, becoming electron depleted in the process as highlighted in Fig. 2(b) where the charge density difference in MoS_2 is largely negative. As a result, its bands shift downward to align more closely with those of (001)-CdS depicted clearly in Fig. 1(b). Conversely, in the (100)-CdS/MoS_2 case, it is the CdS layer that screens the dipole, leaving the band edges of MoS_2 largely unchanged as shown by the relatively neutral charge density difference across the MoS_2 region in Fig. 2(b). This modulation of band edges gives rise to a type-III band alignment in (001)-CdS/MoS_2 in which the bands of MoS_2 are below that of CdS, and a homojunction-like alignment in (100)-CdS/MoS_2 in which the bandgaps of MoS_2 and CdS are nearly identical with minimal band offset as shown in Fig. 3. These assignments are further supported from density of states presented in Fig. S6. In the (001)-CdS/MoS_2 heterostructure, the band offset between the conduction band minimum of MoS_2 and the valence band maximum of CdS is relatively small, at around 30 meV. We note that this assignment is sensitive to variations in the strain of MoS_2, thermal fluctuations, and solvation effects, which are expected to further re-normalize the band edges and remain active topics of investigation. Nevertheless, these findings are in contrast with the type-II band alignments predicted for both heterostructures based on isolated components in Fig. 1, highlighting the limitations of Anderson's rule in predicting band alignment.[57] In particular, the ultrathin nature of the MoS_2 monolayer limits its ability to screen interfacial dipole moments, resulting in substantial band edge renormalization. Similar

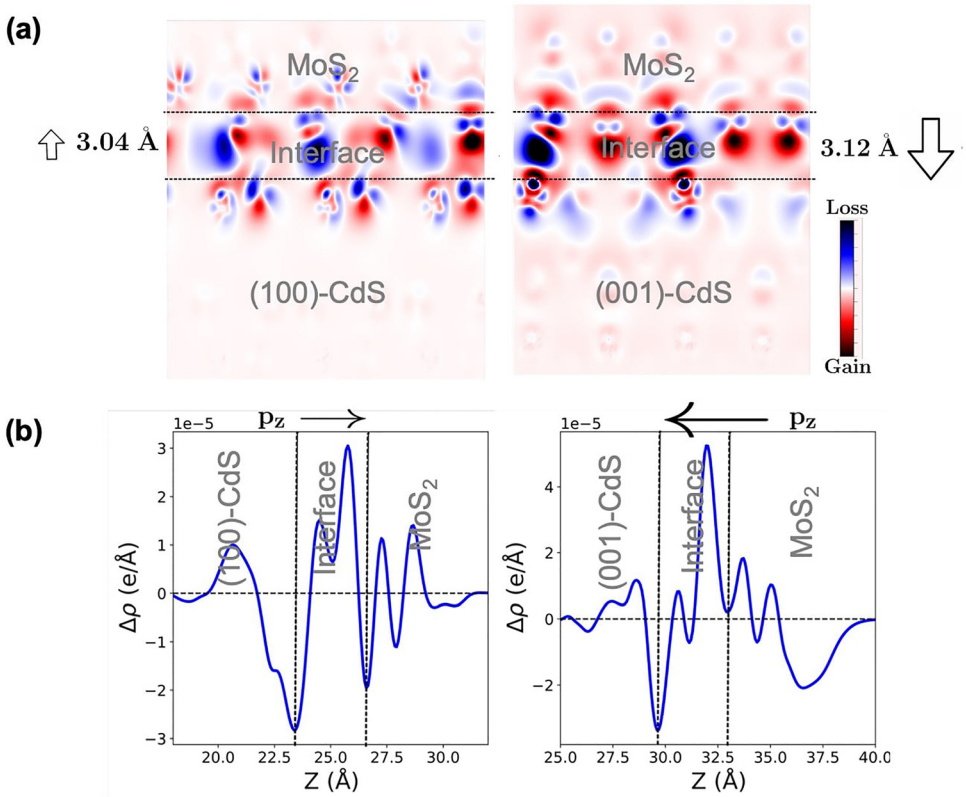

Fig. 2 (a) Charge density difference plot ($\Delta\rho = \rho_{CdS/MoS_2} - \rho_{CdS} - \rho_{MoS_2}$) and interlayer distances for the (001)-CdS/MoS_2 and (100)-CdS/MoS_2 systems. Red and blue regions indicate electron gain and loss, respectively. The dotted lines mark the position of the heterojunction interface. The arrows highlight the strength and direction of the interfacial dipole moment ($\mathbf{p}_z$). (b) Planar-averaged charge density difference profile averaged along the z-axis.

Open Access Article. Published on 22 September 2025. Downloaded on 1/19/2026 9:23:49 PM.
This article is licensed under a Creative Commons Attribution 3.0 Unported Licence.

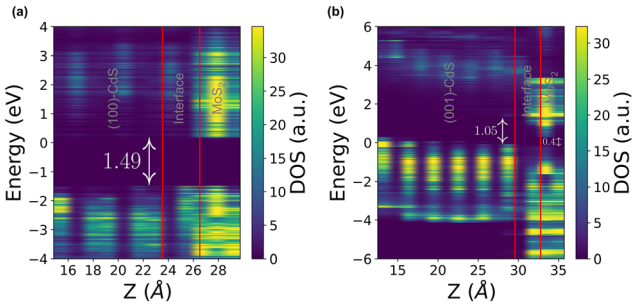

Fig. 3 Spatially resolved density of states (SRDOS) for the (a) (001)-CdS/MoS_2 and (b) (100)-CdS/MoS_2 systems. DOS intensity is mapped to a color for each energy level (with respect to the Fermi level) and position along the z-axis of the heterostructure. The interfacial region is marked by the red lines. CdS and MoS_2 regions are marked accordingly along with the corresponding band gaps.

observations have been reported in other systems, such as BiFeO3/MoS2[58] and (0001)-GaN/MoS_2,[59] where interfacial dipole effects alter the expected alignment. These observations underscore the necessity of explicitly modeling the interface to capture the electrostatic and electronic interactions that govern the actual band alignment in heterostructures.

The type-III alignment observed in (001)-CdS/MoS_2 facilitates charge separation, enabling electron transfer and accumulation on MoS_2. This is consistent with the time-dependent DFT (TDDFT) study by Cheng *et al.*,[22] who observed a two-stage increase in transferred electron density on MoS_2–an initial slow rise attributed to electron–phonon coupling, followed by a rapid 10% increase within 20 fs. They linked this acceleration to the formation of an interfacial dipole that shifts MoS_2 states downward relative to CdS, enabling direct electronic state intermixing. This electron transfer pathway is further corroborated by transient absorption (TA) spectroscopy measurements,[60,61] which observe similar ultrafast carrier dynamics across the CdS/MoS_2 interface. Taken together, these theoretical and experimental findings reinforce our conclusion that the pronounced interfacial dipole in (001)-CdS/MoS_2 plays an important role in modulating band alignment and driving rapid interfacial electron transfer. Additionally, as highlighted in Fig. S5, the band renormalization in (001)-CdS/MoS_2 results in band gap narrowing in both MoS_2 and CdS, which may enable the absorption of low-energy photons. However, the close proximity between the VBM of (001)-CdS and CBM of MoS_2 enables band-to-band tunneling, which can increase the likelihood of interfacial recombination.[62]

The homojunction-like band alignment in the (100)-CdS/MoS_2 heterojunction provides little driving force for charge carrier separation. However, interfacing MoS_2 with the (100)-CdS surface results in a band gap increase of approximately 0.01 eV compared to the isolated (100)-CdS surface. In this configuration, the CBM is positioned above the H^+/H_2 reduction potential and VBM below the H_2O/O_2 oxidation potential, as shown in Fig. 1. While the difference lies within the estimated 10 meV convergence threshold of the calculated band edges—determined from DOS sampling—the (100)-CdS/MoS_2 interface exhibits more favorable band alignment with the water redox potentials, suggesting enhanced suitability for photocatalytic hydrogen evolution.[63] This band gap widening leads to a more favorable band edge alignment with the water redox potentials, in support that (100)-CdS/MoS_2 is a promising candidate for photocatalytic hydrogen evolution.[63] These findings are further supported by the DFT study of Zhang *et al.*, which reported that the (100)-CdS/MoS_2 heterojunction exhibits superior photo-catalytic performance compared to (001)-CdS/MoS_2, attributed to its extended light absorption edge, faster charge carrier mobility, and enhanced visible light absorption.[21]

Based on these findings, we propose that the two CdS facets may act synergistically to enhance photocatalytic activity. The (001)-CdS facet promotes spatial separation of photogenerated charge carriers, while its band gap narrowing extends the light absorption range into the lower-energy region of the spectrum. In contrast, the (100)-CdS facet retains a larger band gap, enabling absorption of higher-energy photons and providing band edge positions well-aligned with the redox potentials required for water splitting reactions.

3.3 Sulfur vacancies in the CdS/MoS_2 heterostructure

In this section, we investigate the influence of sulfur vacancies on the CdS/MoS_2 heterostructure. Specifically, sulfur vacancies on top of the MoS_2 monolayer facing the vacuum positioned above a Cd atom, above a S atom, and within a hollow site are highlighted in Fig. S3. For (001)-CdS/MoS_2, although the introduction of sulfur vacancies leads to an overall charge redistribution at the interface, the local charge environment around the vacancies remains relatively consistent across different defect positions as shown in Fig. 4(a). This is reflected in the Bader charge difference (ΔQ) between the sulfur atoms directly beneath the vacancies before and after geometry optimization, which varies by no more than 0.006 e, indicating that the effect of the sulfur vacancy is uniformly distributed in this facet. By contrast, sulfur vacancies in (100)-CdS/MoS_2 produce qualitatively different charge density difference profiles, with the local ΔQ values varying by up to 0.055 e-nearly an order of magnitude greater than in the (001)-facet. To further quantify these observations, we present the planar-averaged charge density difference profiles in Fig. 4(b). For all sulfur vacancy configurations in (001)-CdS/MoS_2, the interfacial dipole moments consistently point in the same direction, aiding in the electron accumulation on the CdS. Conversely, (100)-CdS/MoS_2 exhibits a more diverse charge redistribution behavior with respect to different locations of the sulfur vacancy, consistent with the qualitatively different two-dimensional profiles among the three sulfur vacancy locations. Specifically, only the sulfur vacancy above the Cd atom leads to a dipole moment that favors electron accumulation on CdS, while those on the S atom and hollow site promote electron accumulation on MoS_2 – the desired outcome for facilitating charge separation. These findings highlight that charge redistribution and the associated energetics induced by sulfur vacancies are facet-dependent, with (100)-CdS/MoS_2 showing more sensitive, localized responses when compared to the (001) facet.

Next, we plot the band edges of the heterostructures containing sulfur vacancies to assess the impact of these defects on band alignment. In the (001)-CdS/MoS_2 system shown in Fig.

Open Access Article. Published on 22 September 2025. Downloaded on 1/19/2026 9:23:49 PM.
This article is licensed under a Creative Commons Attribution 3.0 Unported Licence.

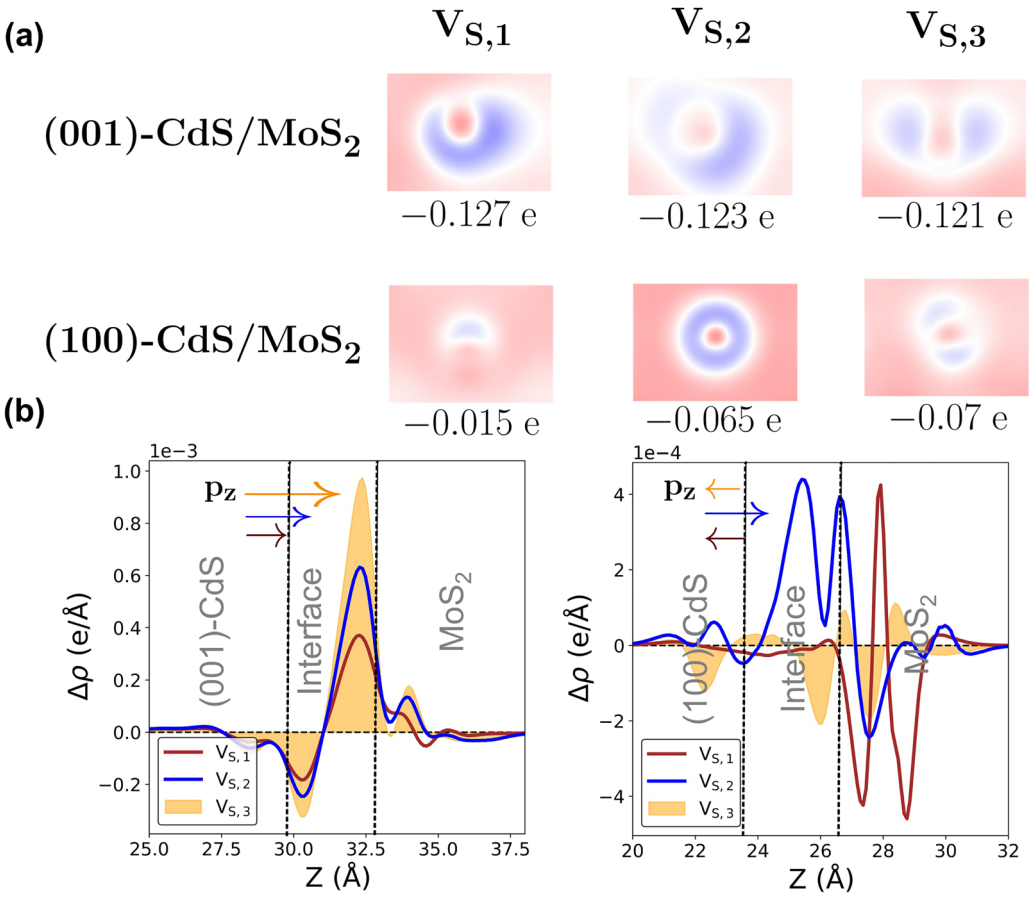

Fig. 4 (a) Local charge density difference ($\Delta\rho = \rho_{CdS/MoS_2} - \rho_{CdS} - \rho_{MoS_2}$) profiles viewed along the z-axis of sulfur atoms directly below various sulfur vacancies for the (001)- and (100)-CdS/MoS_2 heterostructures. Bader charge difference of these sulfur atoms before and after geometry optimization is given below the profiles in number of electrons. Red and blue regions indicate electron gain and loss, respectively. (b) Planar-averaged charge density difference profiles averaged along the z-axis. The CdS side, MoS_2 side, and interface of the heterojunction are marked. The colored arrows indicate the relative magnitudes and directions of interfacial dipole moments ($\mathbf{p}_z$) for the various defects. Sulfur vacancy position notation is given in Fig. S3.

S7a, the introduction of sulfur vacancies does not induce significant changes to the overall electronic structure. Notably, the type-III band alignment observed in the pristine interface is preserved, with the CBM of MoS_2 remaining below the VBM of CdS. Sulfur vacancies cause a slight reduction in the band offset between these states to approximately 10 meV–about 20 meV lower than in the pristine system. This small change appears to be largely independent of the specific vacancy site, consistent with previously observed uniform charge redistribution trends. Although the reduction in band offset is minimal and comparable to thermal energy at room temperature, it could potentially enhance electronic coupling across the interface, which in turn may increase the likelihood of recombination. However, given the subtlety of this effect, detailed calculations of electronic coupling and recombination dynamics are necessary to fully assess its impact on photo-catalytic performance. Similarly, sulfur vacancies in the (100)-CdS/MoS_2 system do not alter the homojunction-like alignment, as shown in Fig. S6b. However, we observe that these vacancies introduce defects states 0.15 and 0.1 eV below the CBM for sulfur vacancies located on top of the Cd atom and S atom, respectively, as highlighted in Fig. 5.

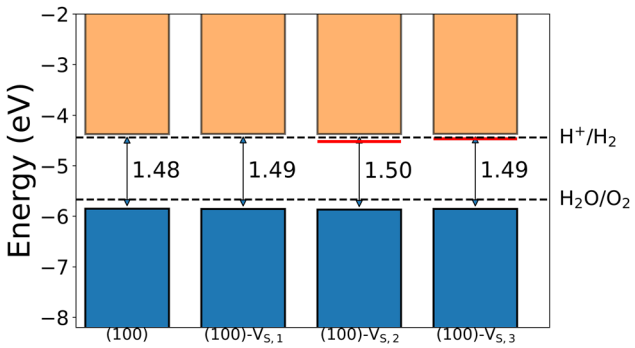

Fig. 5 Conduction (orange) and valence (blue) band edges plotted with respect to vacuum. Defect states are plotted in red. The second defect configuration, corresponding to a sulfur vacancy above a Cd atom, is most stable for (100)-CdS/MoS_2 (see Fig. 6). Notation used is (CdS surface interfaced with MoS_2)-defect number (see Fig. S3 for structures corresponding to defect numbering). Corresponding band gap values (in eV) are given between the band edges. The redox potentials of water are indicated by the dotted lines.

Open Access Article. Published on 22 September 2025. Downloaded on 1/19/2026 9:23:49 PM.
This article is licensed under a Creative Commons Attribution 3.0 Unported Licence.

The small energy separation between the defect states and the CBM may suggest that these are shallow in nature, with a predominantly Mo d-orbital character as illustrated in Fig. S7b.

These defects have several critical effects on photocatalytic performance. Since the associated defect levels lie below the CBM, they can extend the material's photoresponse by enabling sub-bandgap photon absorption, allowing the capture of longer-wavelength light.[29] In addition, these shallow defect states can act as electron traps,[64,65] temporarily localizing charge carriers and thereby suppressing rapid electron–hole recombination. When the energy levels of these traps are favorably aligned near the H^+/H_2 reduction potential, they may also serve as active sites for facilitating the hydrogen evolution reaction (HER), particularly in systems like (100)-CdS/MoS_2. For example, sulfur vacancies in MoS_2 have been shown to activate its inert basal plane by tuning the free energy of adsorption of hydrogen adsorption free energy closer to null.[31,32] Shallow defects induced by anion vacancies have been shown to enhance photocatalytic efficiency in other systems, such as g-C3N4/MoS2,[66] where trap states facilitated interfacial electron transfer, and TiO2,[67] where surface defects suppress charge recombination and broaden the spectral absorption range. We note, however, that a more conclusive identification of HER active sites would require a detailed analysis of water adsorption geometries and reaction pathways, including associated energy barriers.

Given the role of defects in facilitating directional interfacial charge transfer and enhancing the HER on (100)-CdS/MoS_2, we explore the potential of defect engineering as a viable strategy to boost photocatalytic performance. To this end, we compute and compare the formation energies of various intrinsic defects, as shown in Fig. 6. Our results reveal that the sulfur vacancy above the Cd atom yields the most stable sulfur vacancy formation on both (100)- and (001)-CdS/MoS_2, with the former being consistently more favorable by ∼1.5 eV across all configurations. This substantial energy difference suggests that sulfur vacancies are more likely to form at the MoS_2 layer when interfaced with the (100) facet of CdS compared to the (001) facet. This difference may be attributed to strain effects. As noted earlier, the (100)-CdS/MoS_2 heterostructure induces compressive strain in the MoS_2 monolayer, whereas (001)-CdS/MoS_2 induces tensile strain. Previous studies have shown that compressive strain lowers the sulfur vacancy formation energy in MoS_2, while tensile strain increases it.[68,69] This trend is consistent with the lower vacancy formation energy observed for (100)-CdS/MoS_2. The energy differences among individual defect configurations for each of the two facets are relatively small (less than ∼110 meV), making precise site-selective defect control difficult. Nevertheless, the pronounced contrast in defect energetics between the (100) and (001) facets has clear implications. In particular, higher concentrations of sulfur vacancies are expected on the (100)-CdS/MoS_2, which correspond to high concentrations of vacancies above S atoms and hollow sites that we find to promote the favorable charge separation. By contrast, while sulfur vacancies at the (001)-CdS/MoS_2 interface are expected to hinder the desired charge separation, they also occur at lower concentrations.

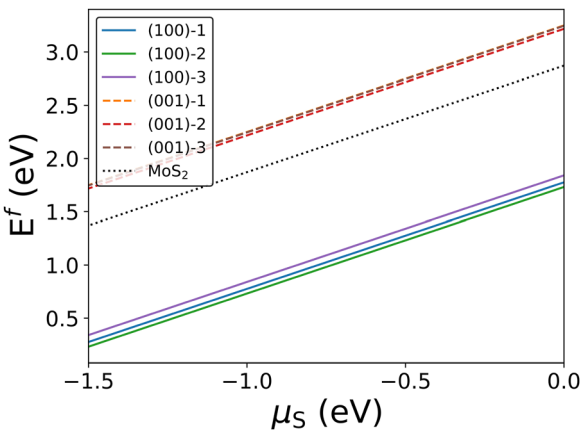

Fig. 6 Formation energies of sulfur vacancies on the CdS surface. The sulfur vacancy above the Cd atom is the most stable for both the (100)- and (001)-CdS/MoS_2 heterojunctions. Notation used is (CdS surface interfaced with MoS_2)-defect number. The formation energy of a sulfur vacancy on monolayer MoS_2 is given by the black dotted line. Sulfur vacancy position notation is given in Fig. S3.

4 Conclusions

In this study, we investigated the role of facet orientation and interfacial point defects on the photocatalytic performance of CdS/MoS_2 heterojunctions. First, we find that the van der Waals heterojunction formation is energetically favorable, inducing interfacial charge redistribution and dipole formation, with a greater magnitude observed for (001)-CdS/MoS_2. This leads to a downwards shift of MoS_2 band edges relative to (001)-CdS due to a combination of strain and screening interactions, while (100)-CdS/MoS_2 exhibits minimal band renormalization. The modulation of band edges results in a type-III alignment for (001)-CdS/MoS_2 and homojunction-like alignment for (100)-CdS/MoS_2. These findings highlight the importance of explicitly modeling the interface to characterize band offsets. In particular, we find that the CBM of the (100)-CdS/MoS_2 heterostructure lies above the H^+/H_2 reduction potential and VBM lies below the H_2O/O_2 oxidation potential, which makes it an ideal photocatalyst system for water-splitting reactions.

Based on these findings, we propose that the enhanced photocatalytic activity observed in CdS/MoS_2 arises from a synergistic effect between the two CdS facets. The (001)-CdS facet facilitates spatial separation of photogenerated charge carriers, and its band gap narrowing extends light absorption into lower-energy regions of the spectrum. In contrast, the (100)-CdS facet maintains a wider band gap, allowing absorption of higher-energy photons and offering band edge positions that are well-aligned with the redox potentials necessary for water splitting.

Next, we examined the effect of sulfur vacancies on photocatalytic activity. In (001)-CdS/MoS_2, all vacancy sites exhibited similar charge density difference profiles, characterized by interfacial dipoles that promote electron accumulation on the CdS side. Correspondingly, the introduction of sulfur vacancies does not significantly alter the overall electronic structure, and

Open Access Article. Published on 22 September 2025. Downloaded on 1/19/2026 9:23:49 PM.
This article is licensed under a Creative Commons Attribution 3.0 Unported Licence.

the system retains its type-III band alignment. In contrast, (100)-CdS/MoS_2 shows more varied responses to sulfur vacancies. Vacancies located above the S atom of MoS_2 and at hollow sites lead to charge redistribution patterns that favor electron accumulation on MoS_2 – an effect that may enhance interfacial charge transfer toward active sites. Furthermore, sulfur vacancies positioned directly above Cd and S atoms introduce shallow defect states approximately 0.1 and 0.15 eV below the CBM, respectively. These defect levels are energetically aligned with the H^+/H_2 reduction potential, indicating their potential role in facilitating the hydrogen evolution reactions. Although the energy differences between individual defect configurations within each facet are relatively small, sulfur vacancies can enhance the interfacial dipole moment on (001) surfaces and active sites on (100) surfaces. This presents a practical strategy for tuning photocatalytic activity in CdS/MoS_2 heterostructures through controlled exposure and defect incorporation.

There are several future directions for elucidating ambiguities observed in CdS/MoS_2 band alignment measurements. Experimentally, Mott–Schottky analysis is commonly used to extract the flat-band potentials of CdS and MoS_2 separately, then used to infer band alignment in the heterostructure. However, this method is highly sensitive to measurement conditions such as electrolyte pH[70] and relies on assumptions like the depletion approximation,[71] which may not be valid for monolayer MoS_2. More critically, it neglects interfacial effects such as charge redistribution, which we show play a significant role in re-normalizing the band alignment. Additionally, most CdS/MoS_2 heterostructures reported in the literature are synthesized as nanoparticles rather than atomically precise interfaces, leading to disordered junctions and considerable interfacial strain. This is particularly important for monolayer MoS_2, which exhibits a high deformation potential and is known to be highly sensitive to strain – strongly affecting its band edge positions and, by extension, the overall band alignment.[72] From a theoretical standpoint, thermal effects such as lattice expansion and phonon-induced atomic vibrations, and solvent-induced polarization can shift semiconductor energy levels from few meV[73] to several hundred meV.[74] Accurate modeling of band offsets therefore requires accounting for both thermal and solvation effects as demonstrated in other systems.[75]

Overall, our findings offer a pathway for rational design of facet- and defect-engineered CdS/MoS_2 heterostructures with enhanced photocatalytic performance. The identification of facet selective defect effects and formation energies provides a strategy to selectively stabilize beneficial defects–such as shallow states aligned with the HER potential–while minimizing recombination pathways. More broadly, this work highlights the importance of atomically resolved models in understanding and optimizing complex semiconductor heterojunctions, and it lays the foundation for future experimental and theoretical efforts to control interfacial energetics in photocatalytic systems.

Author contributions

B. K.: formal analysis; writing – original draft; writing – review & editing. R. A.: conceptualization; supervision; writing – review & editing. W. W.: conceptualization; funding acquisition; project administration; supervision; writing – review & editing.

Conflicts of interest

There are no conflicts to declare.

Data availability

The dataset (~3.5 GB) generated and analyzed in the current study is openly available in Zenodo (URL: **https://doi.org/10.5281/zenodo.15712114**). The dataset contains input files, relaxed structure files, charge density difference plots, partially- and spatially-resolved density of states, data related to defect formation energy; each data type is accompanied with an electronic notebook.

Supplementary information contains calculation methods; converged bulk lattice parameters; electronic structure and defect formation energies on CdS surfaces studied, including structural models, strain *versus* band gap, structural surface relaxation, summaries of isolated and heterostructure band alignments, dipole moments of sulfur vacancies, density of states with and without sulfur vacancies. See DOI: **https://doi.org/10.1039/d5tc02423d**.

Acknowledgements

This work is supported by a grant from The Welch Foundation (grant no. F-2172-20230405). The authors acknowledge the Texas Advanced Computing Center (TACC) at The University of Texas at Austin (URL: **https://www.tacc.utexas.edu**) for HPC resources.

References

1 T. Yusaf, M. Laimon, W. Alrefae, K. Kadirgama, H. A. Dhahad, D. Ramasamy, M. K. Kamarulzaman and B. Yousif, *Appl. Sci.*, 2022, **12**, 781.
2 M. Jaradat, O. Alsotary, A. Juaidi, A. Albatayneh, A. Alzoubi and S. Gorjian, *Energies*, 2022, **15**, 9039.
3 M. Ji and J. Wang, *Int. J. Hydrogen Energy*, 2021, **46**, 38612–38635.
4 S. J. Peighambardoust, S. Rowshanzamir and M. Amjadi, *Int. J. Hydrogen Energy*, 2010, **35**, 9349–9384.
5 C. Acar and I. Dincer, *J. Cleaner Prod.*, 2019, **218**, 835–849.
6 K. Schmietendorf, J. Peinke and O. Kamps, *Eur. Phys. J. B*, 2017, **90**, 1–6.
7 P. Zhou, I. A. Navid, Y. Ma, Y. Xiao, P. Wang, Z. Ye, B. Zhou, K. Sun and Z. Mi, *Nature*, 2023, **613**, 66–70.
8 A. Mills and S. Le Hunte, *J. Photochem. Photobiol., A*, 1997, **108**, 1–35.
9 A. Pan and X. Zhu, *Semiconductor Nanowires*, Elsevier, 2015, pp. 327–363.
10 H. Matsumoto, T. Sakata, H. Mori and H. Yoneyama, *J. Phys. Chem.*, 1996, **100**, 13781–13785.

 This journal is © The Royal Society of Chemistry 2025

Open Access Article. Published on 22 September 2025. Downloaded on 1/19/2026 9:23:49 PM.
This article is licensed under a Creative Commons Attribution 3.0 Unported Licence.

11 L. Wei, Z. Guo and X. Jia, *Catal. Lett.*, 2021, **151**, 56–66.
12 D. Fermín, E. Ponomarev and L. Peter, *J. Electroanal. Chem.*, 1999, **473**, 192–203.
13 J. Low, J. Yu, M. Jaroniec, S. Wageh and A. A. Al-Ghamdi, *Adv. Mater.*, 2017, **29**, 1601694.
14 X. Zong, H. Yan, G. Wu, G. Ma, F. Wen, L. Wang and C. Li, *J. Am. Chem. Soc.*, 2008, **130**, 7176–7177.
15 T. F. Jaramillo, K. P. Jørgensen, J. Bonde, J. H. Nielsen, S. Horch and I. Chorkendorff, *Science*, 2007, **317**, 100–102.
16 Y. Liu, Y.-X. Yu and W.-D. Zhang, *J. Phys. Chem. C*, 2013, **117**, 12949–12957.
17 Y. Min, G. He, Q. Xu and Y. Chen, *J. Mater. Chem. A*, 2014, **2**, 2578–2584.
18 F. Ma, Y. Wu, Y. Shao, Y. Zhong, J. Lv and X. Hao, *Nano Energy*, 2016, **27**, 466–474.
19 Y. Zhong, G. Zhao, F. Ma, Y. Wu and X. Hao, *Appl. Catal., B*, 2016, **199**, 466–472.
20 X. Lian, M. Niu, Y. Huang and D. Cheng, *J. Phys. Chem. Solids*, 2018, **120**, 52–56.
21 J.-R. Zhang, Y.-Q. Zhao, L. Chen, S.-F. Yin and M.-Q. Cai, *Appl. Surf. Sci.*, 2019, **469**, 27–33.
22 K. Cheng, H. Wang, J. Bang, D. West, J. Zhao and S. Zhang, *J. Phys. Chem. Lett.*, 2020, **11**, 6544–6550.
23 K. Chang, M. Li, T. Wang, S. Ouyang, P. Li, L. Liu and J. Ye, *Adv. Energy Mater.*, 2015, **5**, 1402279.
24 L. Lin, S. Huang, Y. Zhu, B. Du, Z. Zhang, C. Chen, X. Wang and N. Zhang, *Dalton Trans.*, 2019, **48**, 2715–2721.
25 G. He, Y. Zhang and Q. He, *Catalysts*, 2019, **9**, 379.
26 K. Hamid, M. Z. B. Mukhlish and M. T. Uddin, *RSC Adv.*, 2024, **14**, 38908–38923.
27 W. Zheng, W. Feng, X. Zhang, X. Chen, G. Liu, Y. Qiu, T. Hasan, P. Tan and P. A. Hu, *Adv. Funct. Mater.*, 2016, **26**, 2648–2654.
28 X. Liu, J. Li and W. Yao, *ACS Omega*, 2020, **5**, 27463–27469.
29 H. Yu, L. Qu, M. Zhang, Y. Wang, C. Lou, Y. Xu, M. Cui, Z. Shao, X. Liu and P. Hu, *et al.*, *Adv. Opt. Mater.*, 2023, **11**, 2202341.
30 S. Bai, N. Zhang, C. Gao and Y. Xiong, *Nano Energy*, 2018, **53**, 296–336.
31 C. Tsai, H. Li, S. Park, J. Park, H. S. Han, J. K. Nørskov, X. Zheng and F. Abild-Pedersen, *Nat. Commun.*, 2017, **8**, 15113.
32 H. Li, C. Tsai, A. L. Koh, L. Cai, A. W. Contryman, A. H. Fragapane, J. Zhao, H. S. Han, H. C. Manoharan and F. Abild-Pedersen, *et al.*, *Nat. Mater.*, 2016, **15**, 48–53.
33 T. G. Edossa and M. M. Woldemariam, *Adv. Condens. Matter Phys.*, 2020, **2020**, 4693654.
34 S.-H. Wei and S. Zhang, *Phys. Rev. B: Condens. Matter Mater. Phys.*, 2000, **62**, 6944.
35 H.-P. Komsa and A. V. Krasheninnikov, *Phys. Rev. B: Condens. Matter Mater. Phys.*, 2015, **91**, 125304.
36 T. Böker, R. Severin, A. Müller, C. Janowitz, R. Manzke, D. Voß, P. Krüger, A. Mazur and J. Pollmann, *Phys. Rev. B: Condens. Matter Mater. Phys.*, 2001, **64**, 235305.
37 J. Y. Rempel, B. L. Trout, M. G. Bawendi and K. F. Jensen, *J. Phys. Chem. B*, 2005, **109**, 19320–19328.
38 M. Pashley, *Phys. Rev. B: Condens. Matter Mater. Phys.*, 1989, **40**, 10481.
39 H. Cornelissen, D. Cammack and R. Dalby, *J. Vac. Sci. Technol., B: Microelectron. Process. Phenom.*, 1988, **6**, 769–772.
40 A. Kokalj and M. Causà, *J. Phys.: Condens. Matter*, 1999, **11**, 7463.
41 Y. Ma, Y. Dai, W. Wei, X. Liu and B. Huang, *J. Solid State Chem.*, 2011, **184**, 747–752.
42 A. S. Barnard and H. Xu, *J. Phys. Chem. C*, 2007, **111**, 18112–18117.
43 K. Sasaki, *Jpn. J. Appl. Phys.*, 1974, **13**, 933.
44 R. Minibaev, A. Bagatur'yants and D. Bazhanov, *Nanotechnol. Russ.*, 2010, **5**, 191–197.
45 K. L. Kavanagh, *Semicond. Sci. Technol.*, 2010, **25**, 024006.
46 P. Giannozzi, S. Baroni, N. Bonini, M. Calandra, R. Car, C. Cavazzoni, D. Ceresoli, G. L. Chiarotti, M. Cococcioni and I. Dabo, *et al.*, *J. Phys.: Condens. Matter*, 2009, **21**, 395502.
47 D. Hamann, *Phys. Rev. B: Condens. Matter Mater. Phys.*, 2013, **88**, 085117.
48 J. P. Perdew, K. Burke and M. Ernzerhof, *Phys. Rev. Lett.*, 1996, **77**, 3865.
49 S. Grimme, J. Antony, S. Ehrlich and H. Krieg, *J. Chem. Phys.*, 2010, **132**, 154104.
50 K. Santosh, R. C. Longo, R. Addou, R. M. Wallace and K. Cho, *Nanotechnology*, 2014, **25**, 375703.
51 Y. Li, X. Li, C. Yang and Y. Li, *J. Mater. Chem.*, 2003, **13**, 2641–2648.
52 S.-M. Ko, J.-H. Kim, Y.-H. Ko, Y. H. Chang, Y.-H. Kim, J. Yoon, J. Y. Lee and Y.-H. Cho, *Cryst. Growth Des.*, 2012, **12**, 3838–3844.
53 J. Xie, H. Zhang, S. Li, R. Wang, X. Sun, M. Zhou, J. Zhou, X. W. Lou and Y. Xie, *Adv. Mater.*, 2013, **25**, 5807–5813.
54 B. Hinnemann, P. G. Moses, J. Bonde, K. P. Jørgensen, J. H. Nielsen, S. Horch, I. Chorkendorff and J. K. Nørskov, *J. Am. Chem. Soc.*, 2005, **127**, 5308–5309.
55 G. Li, D. Zhang, Q. Qiao, Y. Yu, D. Peterson, A. Zafar, R. Kumar, S. Curtarolo, F. Hunte and S. Shannon, *et al.*, *J. Am. Chem. Soc.*, 2016, **138**, 16632–16638.
56 T. Björkman, A. Gulans, A. V. Krasheninnikov and R. M. Nieminen, *Phys. Rev. Lett.*, 2012, **108**, 235502.
57 R. L. Anderson, *Solid-State Electron.*, 1962, **5**, 341–351.
58 J.-Q. Dai, X.-W. Wang and T.-F. Cao, *J. Phys. Chem. C*, 2019, **123**, 3039–3047.
59 H. Henck, Z. Ben Aziza, O. Zill, D. Pierucci, C. H. Naylor, M. G. Silly, N. Gogneau, F. Oehler, S. Collin and J. Brault, *et al.*, *Phys. Rev. B*, 2017, **96**, 115312.
60 S. Zhang, S. Li, M. Zhou, X. Li, Y. Wang, S. Suo, C. Chen, Z. Zhang, R. Zhang and B. Jin, *et al.*, *Sep. Purif. Technol.*, 2025, **355**, 129664.
61 F. Zhang, Y. Hong, Z. Yao, Y. Li, S. Zheng, S. Yu, A. Yartsev, K. Zheng, T. Pullerits and Y. Zhou, *ACS Appl. Nano Mater.*, 2025, **8**, 11338–11345.
62 C. Gong, H. Zhang, W. Wang, L. Colombo, R. M. Wallace and K. Cho, *Appl. Phys. Lett.*, 2013, **103**, 053513.
63 M. C. Toroker, D. K. Kanan, N. Alidoust, L. Y. Isseroff, P. Liao and E. A. Carter, *Phys. Chem. Chem. Phys.*, 2011, **13**, 16644–16654.

Open Access Article. Published on 22 September 2025. Downloaded on 1/19/2026 9:23:49 PM.
This article is licensed under a Creative Commons Attribution 3.0 Unported Licence.

64 H. F. Haneef, A. M. Zeidell and O. D. Jurchescu, *J. Mater. Chem. C*, 2020, **8**, 759–787.
65 K. W. Böer and U. W. Pohl, *Semiconductor physics*, Springer Nature, 2023.
66 J. Xue, M. Fujitsuka and T. Majima, *ACS Appl. Mater. Interfaces*, 2019, **11**, 40860–40867.
67 G. Dong, X. Wang, Z. Chen and Z. Lu, *Photochem. Photobiol.*, 2018, **94**, 472–483.
68 R. Anvari and W. Wang, *J. Appl. Phys.*, 2024, **135**, 174304.
69 R. Albaridy, D. Periyanagounder, D. Naphade, C.-J. Lee, M. Hedhili, Y. Wan, W.-H. Chang, T. D. Anthopoulos, V. Tung and A. Aljarb, *et al.*, *ACS Mater. Lett.*, 2023, **5**, 2584–2593.
70 S. F. Lee, E. Jimenez-Relinque, I. Martinez and M. Castellote, *Catalysts*, 2023, **13**, 1000.
71 T. Kirchartz, W. Gong, S. A. Hawks, T. Agostinelli, R. C. MacKenzie, Y. Yang and J. Nelson, *J. Phys. Chem. C*, 2012, **116**, 7672–7680.
72 H. Peelaers and C. G. Van de Walle, *Phys. Rev. B: Condens. Matter Mater. Phys.*, 2012, **86**, 241401.
73 Y. Zhang, Z. Wang, J. Xi and J. Yang, *J. Phys.: Condens. Matter*, 2020, **32**, 475503.
74 Y. Ping, R. Sundararaman and W. A. Goddard III, *Phys. Chem. Chem. Phys.*, 2015, **17**, 30499–30509.
75 G. Melani, W. Wang, F. Gygi, K.-S. Choi and G. Galli, *ACS Energy Lett.*, 2024, **9**, 5166–5171.

 This journal is © The Royal Society of Chemistry 2025